

Supplementary Information

Emulation of Neuron and Synaptic Functions in Spin-Orbit Torque Domain Wall Devices

Durgesh Kumar¹, Ramu Maddu¹, Hong Jing Chung², Hasibur Rahaman¹, Tianli Jin¹, Sabpreet Bhatti¹, Sze Ter Lim², Rachid Sbiaa³, S. N. Piramanayagam^{1,*}

¹School of Physical and Mathematical Sciences, Nanyang Technological University, 21 Nanyang Link, Singapore, 637371

²Institute of Materials Research and Engineering, A*STAR, 2 Fusionopolis Way, Innovis, Singapore, 138634

³Department of Physics, Sultan Qaboos University, Muscat, Oman

*prem@ntu.edu.sg

Contents

1. Micromagnetic Simulations: Domain Wall Dynamics in Meander Synaptic Devices.....	2
2. Device Layout.....	3
3. R-H Loops of Meander Domain Wall Devices	4
4. Basics of Anomalous Hall Voltage Measurements	5
5. Current Sweeping Experiments	6
6. Spin-Orbit Torque Driven Domain Wall Motion in Synaptic Device.....	7
7. Micromagnetic Simulations: Domain Wall Dynamics in Neuron Devices	10
8. Spike Neuron: Results at Different Current Densities.....	10
9. Spike and Step Neurons: Results from Different Devices.....	11
10. Video Links.....	13
References	15

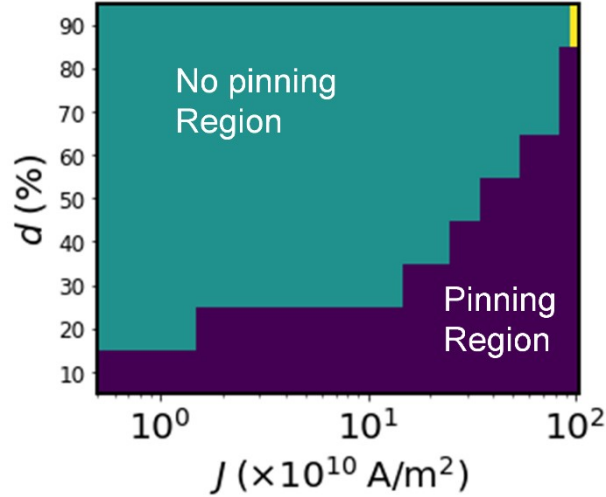
1. Micromagnetic Simulations: Domain Wall Dynamics in Meander Synaptic Devices

Corresponding to figure (1 (b-c)) in the paper, here, we have presented a phase diagram of domain wall (DW) motion in meander devices with one pinning site. Here violet and green colors represent the “pinning” and “no pinning” regions. The yellow color represents the random nucleation of reversed domains that happen at high current density values. We have studied the DW dynamics in a large range of J (1×10^{10} to 1×10^{12} A/m²) and d (10 to 90%). The corresponding phase information is also presented in table 1. Where “p” and “np” represent the “DW pinning” and “no DW pinning”, respectively. The first current density value in the green region is defined as the depinning current density (J_{dep}) and this increases with the increase in the offset value (d).

Table 1. A table containing the details of DW dynamics in meander devices with one pinning site.

J (A/m ²) / d (%)	10	20	30	40	50	60	70	80	90
1×10^{10}	np	p	p	p	p	p	p	p	p
2×10^{10}	np	np	p	p	p	p	p	p	p
3×10^{10}	np	np	p	p	p	p	p	p	p
4×10^{10}	np	np	p	p	p	p	p	p	p
5×10^{10}	np	np	p	p	p	p	p	p	p
6×10^{10}	np	np	p	p	p	p	p	p	p
7×10^{10}	np	np	p	p	p	p	p	p	p
8×10^{10}	np	np	p	p	p	p	p	p	p
9×10^{10}	np	np	p	p	p	p	p	p	p
1×10^{11}	np	np	p	p	p	p	p	p	p
2×10^{11}	np	np	np	p	p	p	p	p	p
3×10^{11}	np	np	np	np	p	p	p	p	p
4×10^{11}	np	np	np	np	np	p	p	p	p
5×10^{11}	np	np	np	np	np	p	p	p	p
6×10^{11}	np	np	np	np	np	np	p	p	p
7×10^{11}	np	np	np	np	np	np	p	p	p
8×10^{11}	np	np	np	np	np	np	p	p	p
9×10^{11}	np	p							
1×10^{12}	np								

*p: domain wall pinning and np: no domain wall pinning



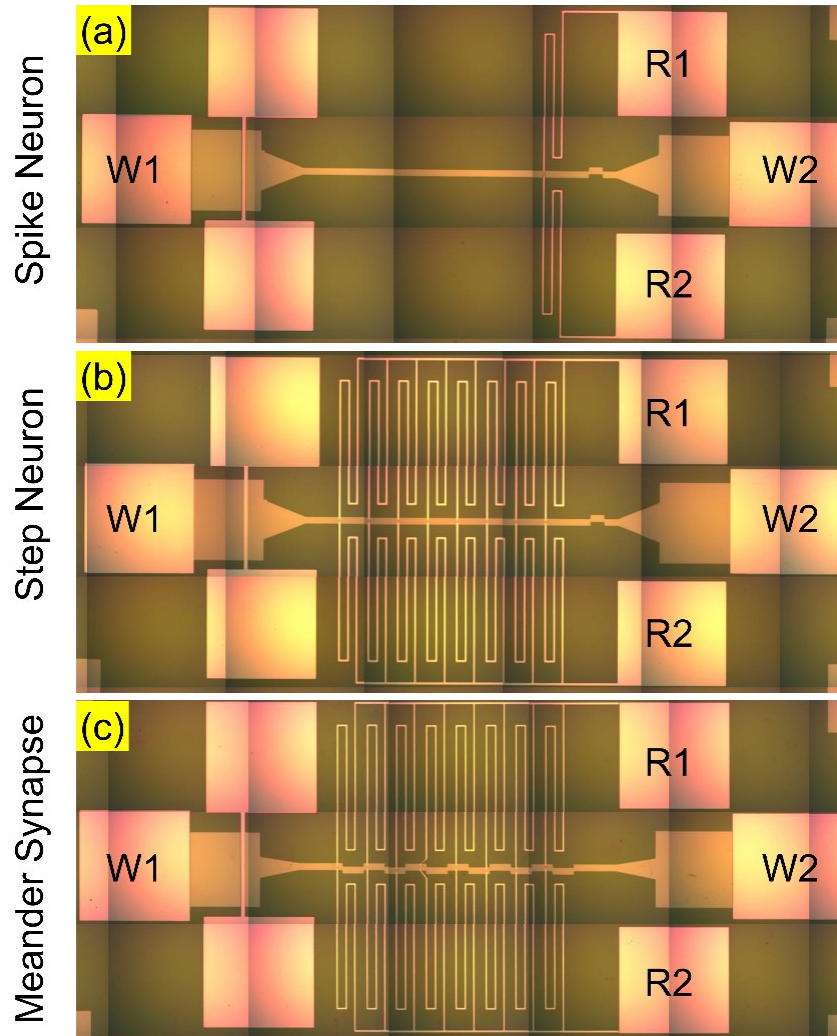
Supplementary Figure 1. Micromagnetic Simulations: The phase diagram of domain wall motion in meander wire with one pinning site.

2. Device Layout

For better understanding of the device designs and Hall bar designs, we present the optical image of the fabricated devices. In the optical micrographs, the small squares represent the smallest field of view of our optical lithography system.

For the spike neuron devices, we fabricated one pair of Hall bars. This is the conventional arrangement. These Hall bars were connected to the two separate electrode pads. We apply the reading current (same as writing current) through the current channel (between W1 and W2, figure 6 (a) of the paper and supplementary figure 2 (a)). The resultant anomalous Hall voltage was measured between the electrode pads connecting the Hall bars (between R1 and R2, figure 6 (a) of the paper and supplementary figure 2 (a)).

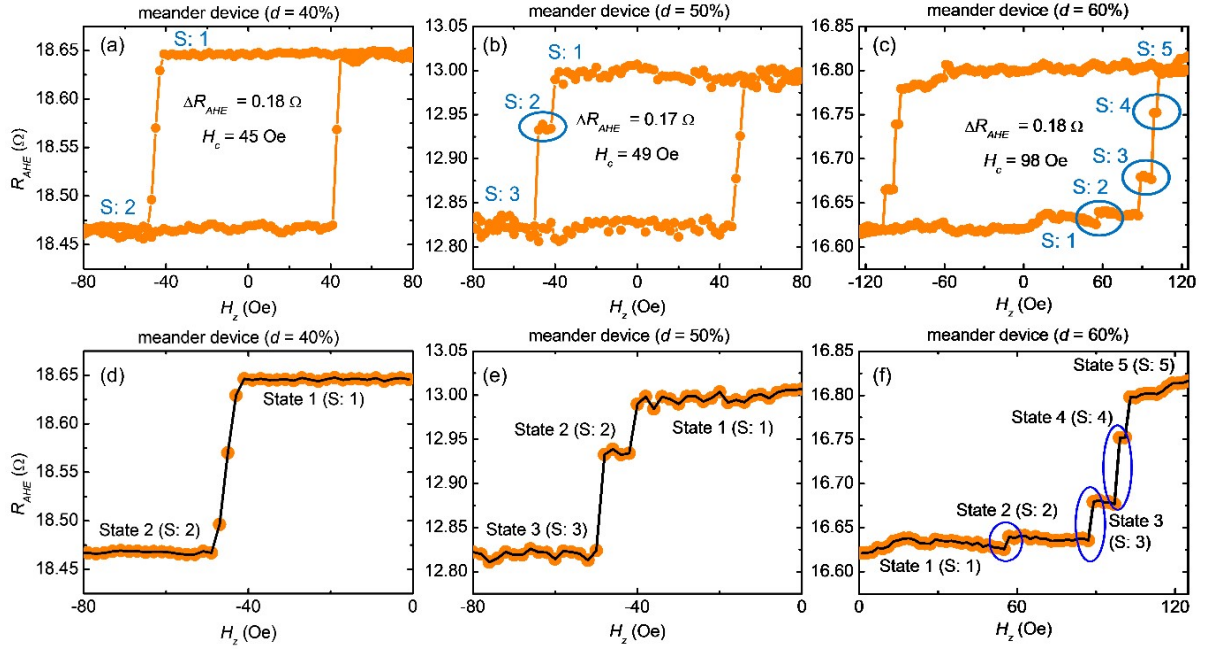
In contrast, in the case of step neuron and meander devices, we fabricated a total of eight pairs of equally spaced Hall bars. 8 Hall bars, connected at one transverse end of the device (say top end) join to a single electrode pad (supplementary figure 2 (b-c)). The other 8 Hall bars connected to the other end of the device (i.e. bottom end) meet the second electrode pad. The anomalous Hall voltage was measured between these two electrode pads (R1 and R2). The current channel is identical to the one described for the spike neuron devices (W1 and W2). Please refer to figure 2 and 6 of the main manuscript and supplementary figure 2 for the detailed illustrations.



Supplementary Figure 2: The optical micrograph illustrating the reading and writing schemes in our domain wall-based neuron and synaptic devices.

3. R-H Loops of Meander Domain Wall Devices

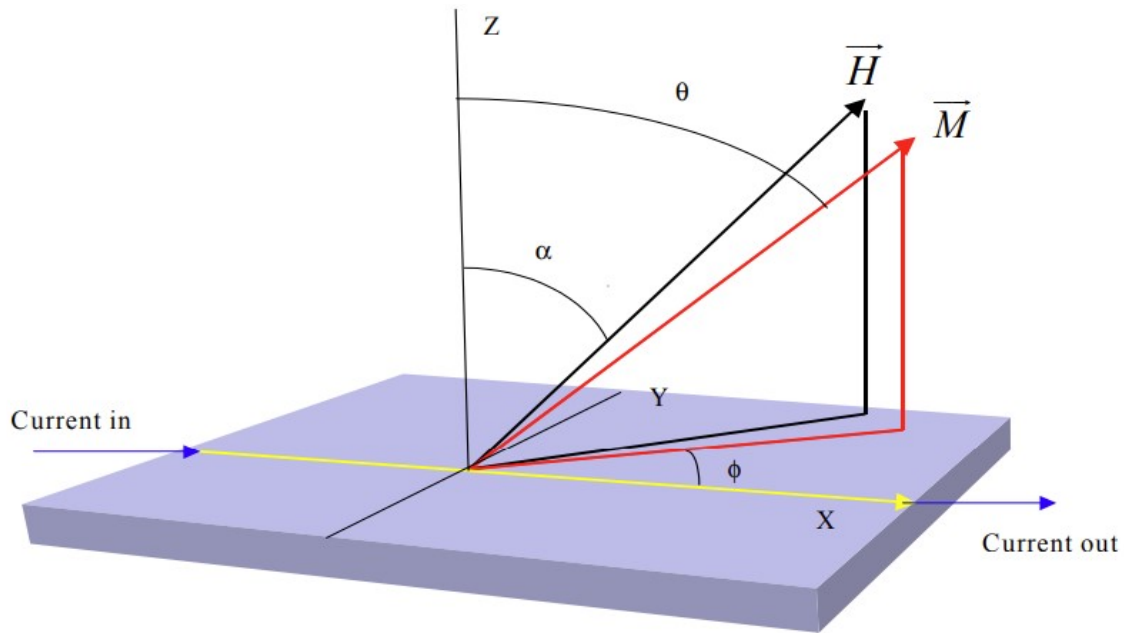
Corresponding to R-H loops presented in the main manuscript, here we present the same result in a more illustrative manner. The experimental details and corresponding discussions are presented in detail in the paper.



Supplementary Figure 3. The R-H loops for meander devices with $d =$ (a & d) 40%, (b & e) 50%, and (c & f) 60%. In supplementary figures 2 (d-f), we have presented the data only for a selected range.

4. Basics of Anomalous Hall Voltage Measurements

To understand the reason for an improved signal in the proposed reading scheme, we presented an explanation in the paper. The explanation requires the discussion of the supplementary figure 4. We, therefore, request our readers to refer to supplementary figure 4 for relevant discussions.

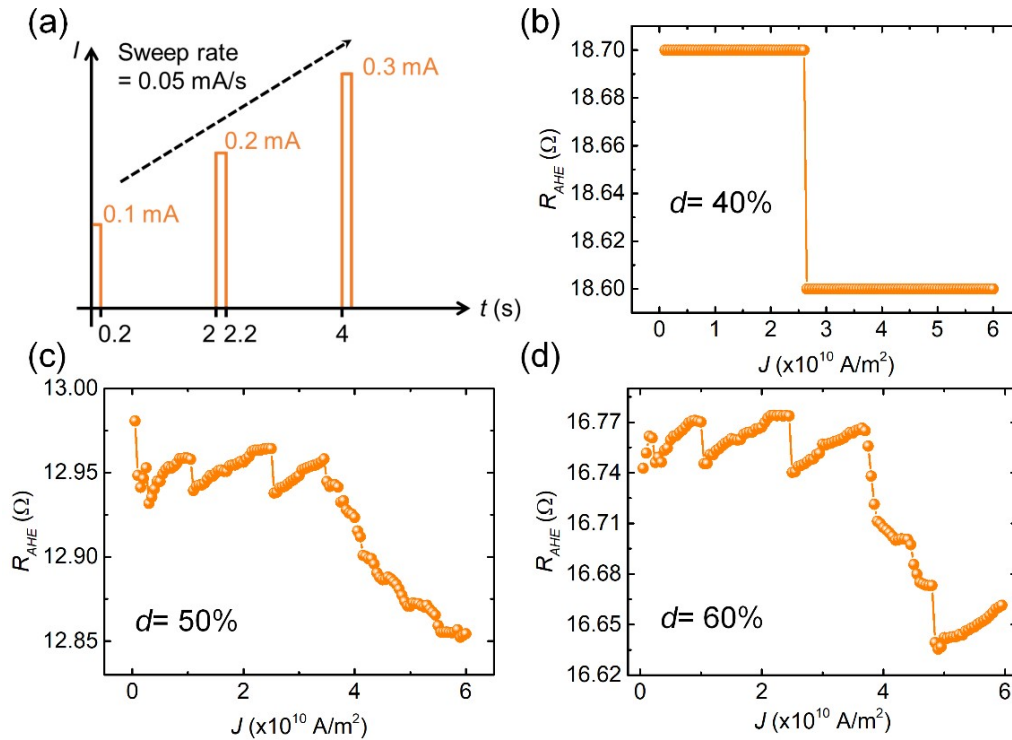


Supplementary Figure 4: The geometrical representation of anomalous Hall effect measurements [1].

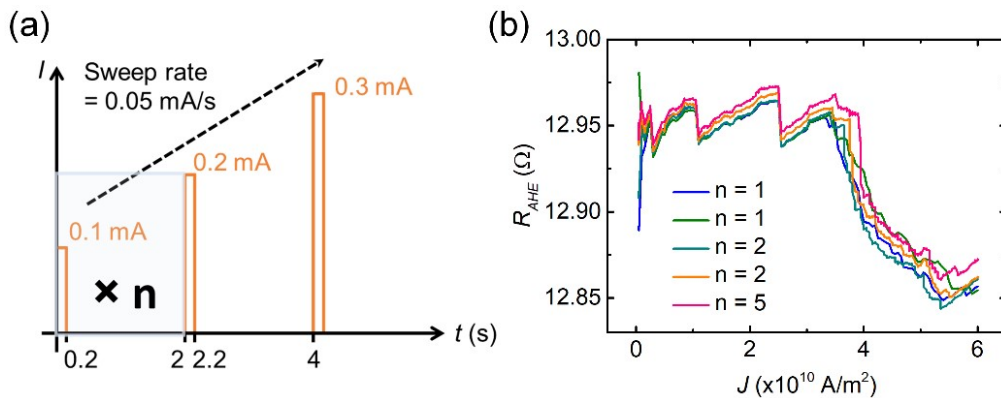
5. Current Sweeping Experiments

We have also studied the magnetization switching while sweeping the electrical current. Like the previous case, we first saturated the samples using a large out-of-plane (OOP) magnetic field of -1000 Oe. Subsequently, we swept the electrical current (in a direction the same as in figure 4 of the paper) at a sweep rate of 0.05 mA/s. A simultaneous longitudinal magnetic field of 500 Oe (in a direction the same as in figure 4 of the paper) was also applied. The writing current was utilized as the reading current with a pulse width of 0.2 s and the resultant transverse voltage was measured using a nano-voltmeter. The experimental procedure is schematically shown in supplementary figure 5 (a). One can see in supplementary figure 5 (b-d) that we could observe the multiple resistance states for $d = 50$ and 60%. As discussed in the paper, an increase in offset also enhances the probability of nucleation of the reversed domain while sweeping the SOT current. Additionally, we also repeated these experiments for $n = 2$ and 5 (supplementary figure 6) and observed similar resistance states. The only difference is that the Joule heating increases as “n” increases.

During the current sweeping experiments, initially, we observe the steps. At higher current densities, the steps in anomalous Hall resistance are not clear. This is because the DW motion is harder to control at higher current densities. This is due to: (a) A continuous increase in the magnitude of the current density causes more Joule heating than the application of current pulses with fixed magnitude. (b) At higher current densities, the DW motion is close to the depinning region. This is the reason; we emphasize more on the DW motion driven by current pulses with constant magnitude in our study.



Supplementary Figure 5. Current Sweeping: (a) Schematic of the experimental procedure. The graph of R_{AHE} vs J for an offset of (b) 40%, (c) 50%, and (d) 60%.

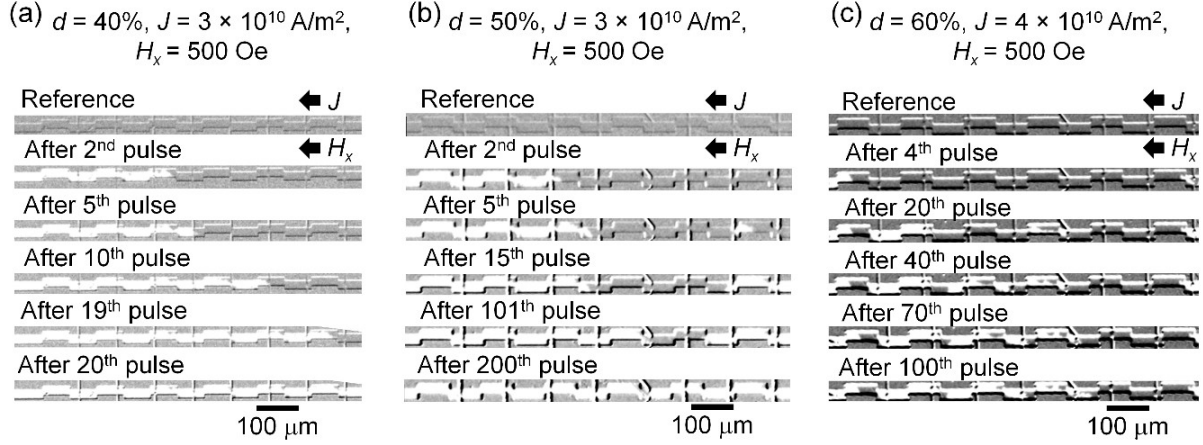


Supplementary Figure 6. Current Sweeping: (a) Schematic of the experimental procedure with $n \geq 1$. (b) The graph of R_{AHE} vs J for different “ n ” values at an offset of 50%.

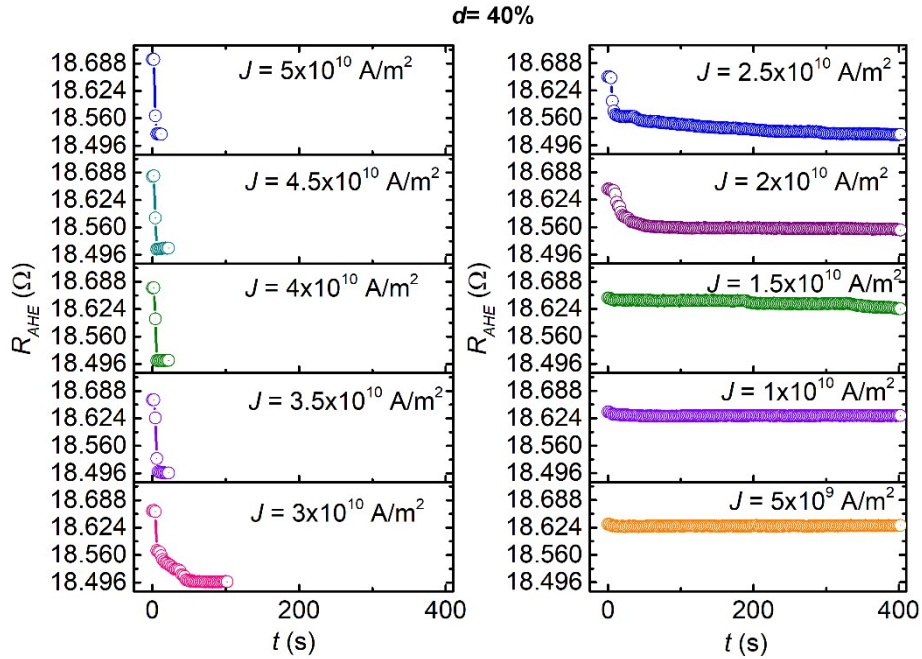
6. Spin-Orbit Torque Driven Domain Wall Motion in Synaptic Device

Supplementary figure 7 presents the Kerr microscopy images of the DW motion in meander devices in response to the pulsed current. The experimental process is the same as the one utilized in figure 3 of the paper. As one can see in supplementary figure 7 (a), when we apply the current pulses of magnitude $3 \times 10^{10} \text{ A/m}^2$ in the presence of an in-plane magnetic field of 500 Oe, a reversed domain nucleates at the left end of the device. In response to the subsequent current pulses, the DW moves towards the right end of the device. The DW stays at the pinning site for a short while. However, the DW pinning is not very strong. When we repeated these experiments for meander devices with an offset of 50%, a similar DW motion was observed. However, the pinning strength increases compared to the case of $d = 40\%$. For $d = 60\%$, the pinning strength is the highest. This aspect will be clearer from supplementary figures (8-10). Also, we observe some random nucleation in the wires. This happens at the pinning sites or the places where Hall bars were deposited. In the first case, it is because the current density increases at the pinning sites. However, the latter produces process-induced nucleation sites. This aspect has been discussed in detail in the paper. The nature of DW motion/magnetization switching is consistent with the SOT-induced DW motion/magnetization switching [2].

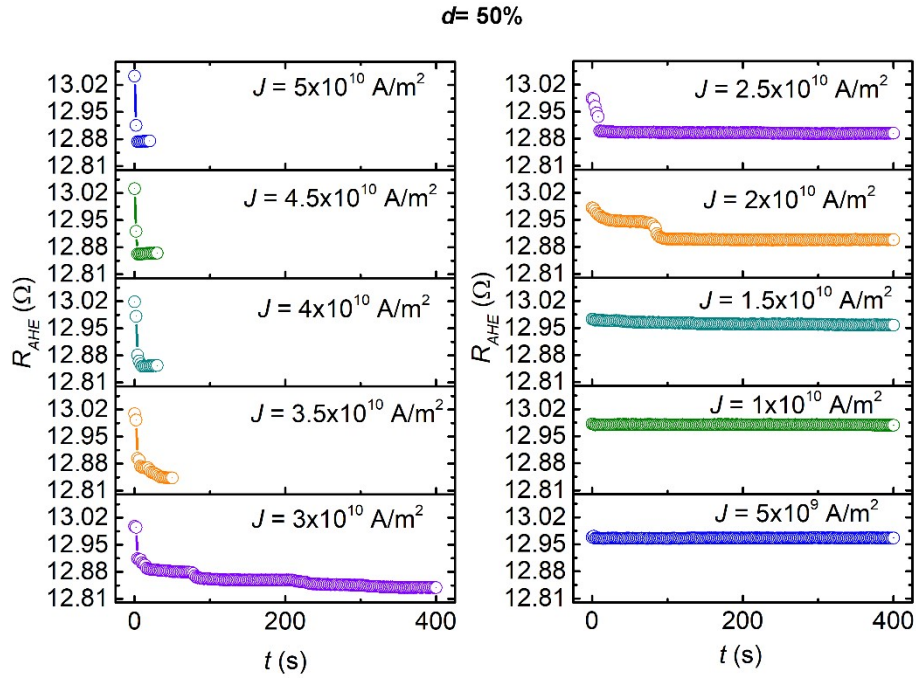
Corresponding to figure 3 in the paper, here, we present details of spin-orbit torque (SOT)-driven DW motion for meander devices with offsets of 40%, 50%, and 60% (supplementary figures 8-10). We present the results of all the studied current density values. The “no domain wall motion”, “domain wall pinning”, and “domain wall depinning” regions are also demonstrated in detail.



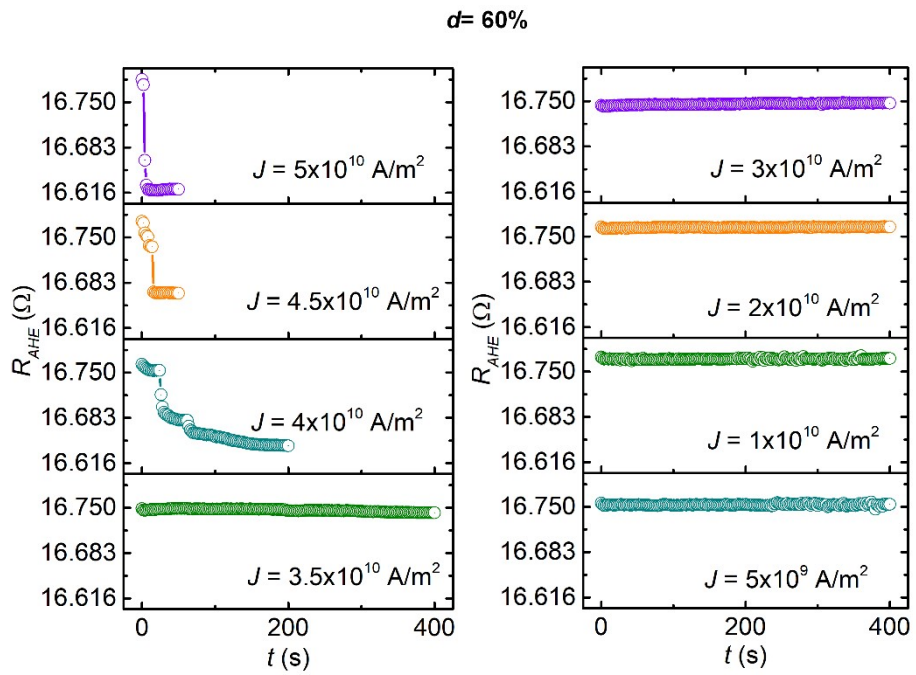
Supplementary Figure 7. SOT Driven Domain Wall Motion: The results of Kerr microscopy and corresponding electrical measurements that illustrate the domain wall dynamics in meander synaptic devices with (a) $d = 40\%$, $J = 3 \times 10^{10} \text{ A/m}^2$, and $H_x = 500 \text{ Oe}$, (b) $d = 50\%$, $J = 3 \times 10^{10} \text{ A/m}^2$, and $H_x = 500 \text{ Oe}$, and (c) $d = 60\%$, $J = 6 \times 10^{10} \text{ A/m}^2$, and $H_x = 500 \text{ Oe}$.



Supplementary Figure 8. SOT Driven Domain Wall Motion: Spin-orbit torque (SOT)-driven domain wall motion for meander devices with $d = 40\%$ at different current densities ranging from 5×10^9 to $5 \times 10^{10} \text{ A/m}^2$.



Supplementary Figure 9. SOT Driven Domain Wall Motion: Spin-orbit torque (SOT)-driven domain wall motion for meander devices with $d = 50\%$ at different current densities ranging from 5×10^9 to 5×10^{10} A/m².



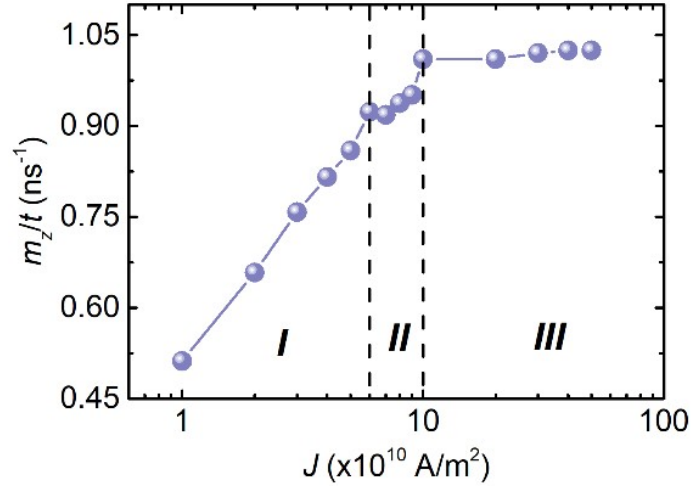
Supplementary Figure 10. SOT Driven Domain Wall Motion: Spin-orbit torque (SOT)-driven domain wall motion for meander devices with $d = 60\%$ at different current densities ranging from 5×10^9 to 5×10^{10} A/m².

7. Micromagnetic Simulations: Domain Wall Dynamics in Neuron Devices

We plotted the “ m_z/t ” ($\propto v$ “domain wall velocity”) as a function of current density “ J ” for a better understanding of DW motion in our neuron devices. The resultant graph can be divided into three regimes (I, II, and III), as shown in supplementary figure 11. In region I, the domain wall velocity increases with the current density. This can be understood using the following relation [3],

$$H_{SOT} = -\frac{\hbar\theta_{SH}J}{2|e|M_s t}(\hat{m} \times \hat{\sigma}) \quad (1)$$

Here, \hbar , θ_{SH} , J , e , M_s and t stand for the reduced Planck constant, spin Hall angle, current density, electronic charge, saturation magnetization, and thickness of the ferromagnetic layer, respectively. In addition, \hat{m} and $\hat{\sigma}$ represent the directions of magnetization inside the domain wall and spin polarization. One can see from equation (1) that the effective spin-orbit torque field increases as current density increases. At a certain current density, the DW velocity slightly drops. This may be related to the Walker breakdown as the SOT can be understood as an effective out-of-plane magnetic field [4], [5], [6], [7]. This is indicated in region II in supplementary figure 11. A further increase in the current density increases the DW velocity. However, beyond a certain current density, the DW velocity saturates. This is the current density at which maximum SOT is achieved and a further increase in current density does not affect the DW velocity. This is defined as region III in supplementary figure 11.

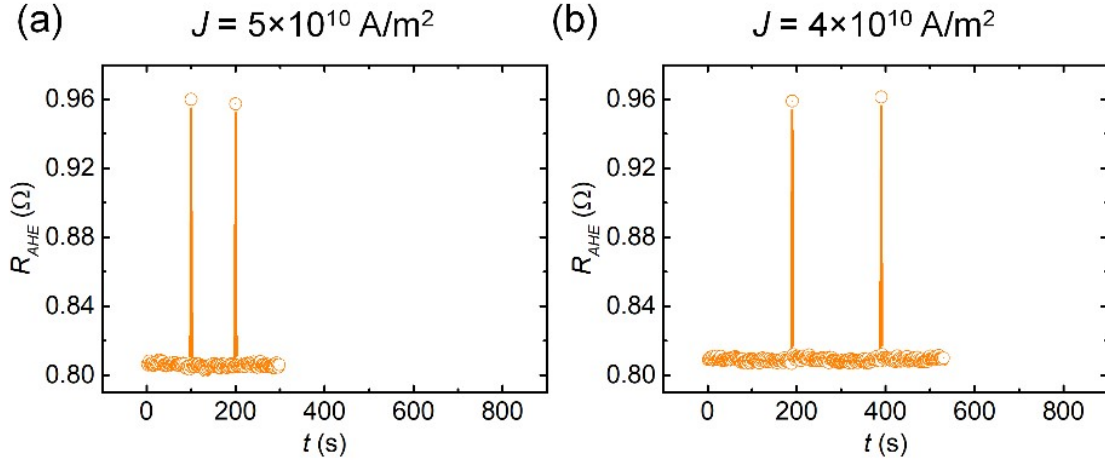


Supplementary Figure 11. Micromagnetic simulations: The graph of m_z/t vs J for neuron devices.

8. Spike Neuron: Results at Different Current Densities

The functionalities of spike neurons at other current density values ($J = 5 \times 10^{10}$ A/m 2 , 4×10^{10} A/m 2 , and 3.5×10^{10} A/m 2) are presented in this section (supplementary figure 12). The

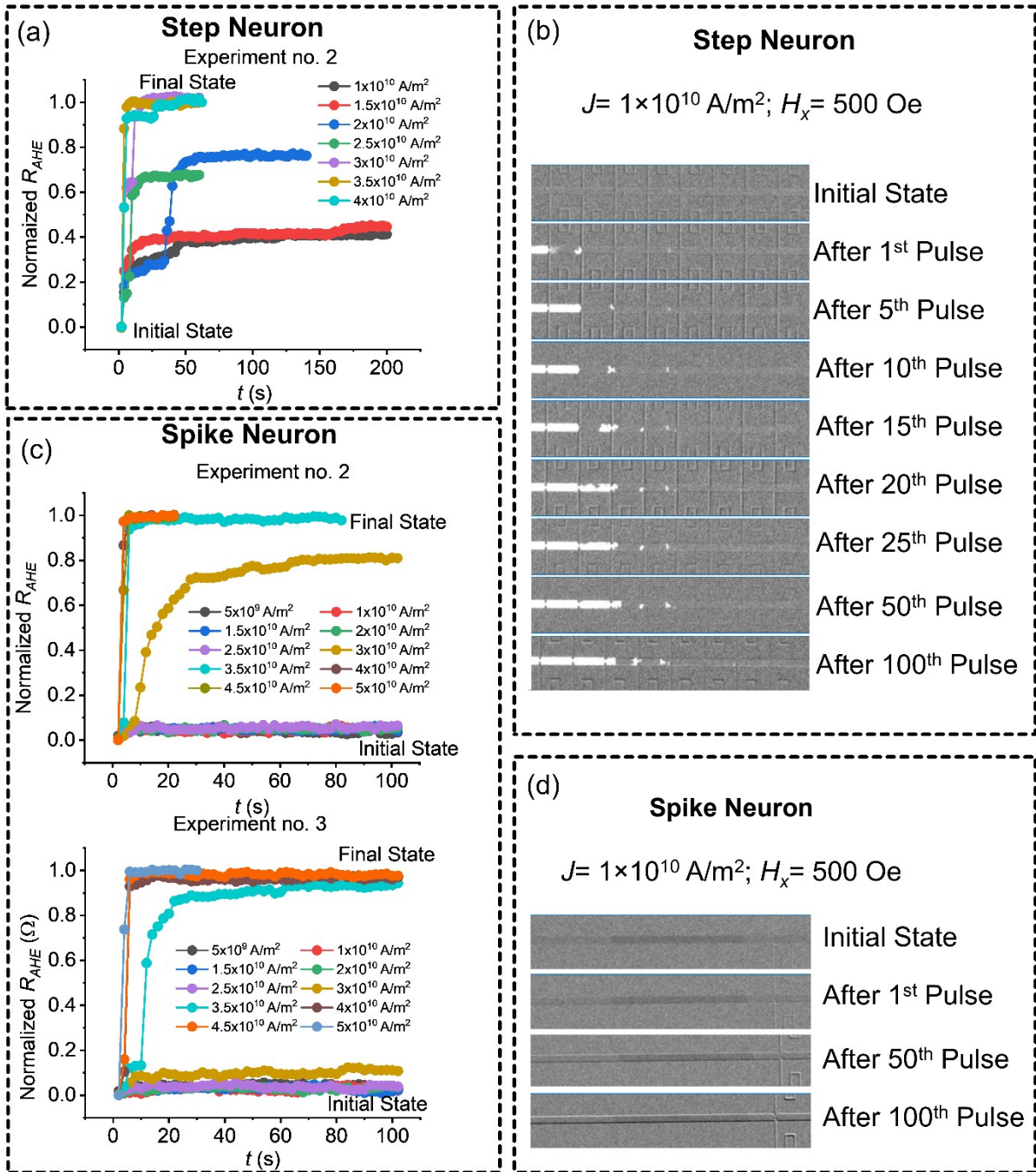
experimental procedure is the same as the one presented in the paper (figure 7). These results also indicate towards the good reproducibility of our experimental results on spike neurons.



Supplementary Figure 12. Results on spike neurons: Demonstration of domain wall dynamics in spike neuron devices for different current densities.

9. Spike and Step Neurons: Results from Different Devices

As we have discussed in the paper, for spike neurons, we mainly observed two regions of DW motion as a function of current density. (a) At low current densities, the DW does not move (or negligible DW motion). (b) At higher current densities, a sharp DW motion was observed. We only observed one intermediate data point. However, in the case of step neurons, the first region (region (a)) of DW motion was missing. We always observed a DW motion (observation of intermediate region for more current density values). At low current densities, a slow and at high current densities a relatively sharper DW motion was observed. Please refer to table III for details of the above discussion. To check, the repeatability of the above observations, we performed the similar experiments on different devices. These results are presented in supplementary figure 13 below. For a better understanding of the data, we have also presented the Kerr microscopy images for step and spike neurons at a current density of 1×10^{10} A/m². A clear difference in the nature of the DW motion, as discussed above, can be seen in supplementary figure 13 (b & d). This is consistent with our results on devices reported in the paper. Overall, we observed similar results in second set of devices as compared to the devices from set 1 (devices which were discussed in the paper).



Supplementary Figure 13. The repeatability test of domain wall dynamics in Step and Spike neuron devices. A clear difference in the nature of the DW motion can be seen in supplementary figure 13 (b & d). This is consistent with our results on devices reported in the paper.

10. Video Links

Meander synapse video

<https://youtu.be/q6OdU6ouDEQ>

Reference wire ($J = 5 \times 10^{11}$ A/m²)

<https://youtu.be/c7QPOVzamj4>

Reference wire ($J = 1 \times 10^{10}$ A/m²)

<https://youtu.be/H1ZfrsizxA>

Meander wire ($d = 10\%$, $J = 5 \times 10^{10}$ A/m²)

<https://youtu.be/s1JWusPs1Co>

Meander wire ($d = 20\%$, $J = 5 \times 10^{10}$ A/m²)

<https://youtu.be/YDhOUdaq-Tw>

Meander wire ($d = 30\%$, $J = 5 \times 10^{10}$ A/m²)

<https://youtu.be/ush-ZHLba9Y>

Meander wire ($d = 40\%$, $J = 5 \times 10^{10}$ A/m²)

<https://youtu.be/PLj7qHEbAsw>

Meander wire ($d = 50\%$, $J = 5 \times 10^{10}$ A/m²)

<https://youtu.be/DcYVv4aWqUY>

Meander wire ($d = 60\%$, $J = 5 \times 10^{10}$ A/m²)

<https://youtu.be/ZhvAGUqf3nE>

Meander wire ($d = 70\%$, $J = 5 \times 10^{10}$ A/m²)

<https://youtu.be/RQFtAHoIW7M>

Meander wire ($d = 80\%$, $J = 5 \times 10^{10}$ A/m²)

<https://youtu.be/ZeuqrGQlzJw>

Meander wire ($d = 90\%$, $J = 5 \times 10^{10}$ A/m²)

<https://youtu.be/HVL2ZDWIUU0>

References

- [1] “https://www.lakeshore.com/docs/default-source/about-us-document-library/publications/anomalous_hall1.pdf?sfvrsn=d144a797_1”.
- [2] D. Kumar *et al.*, “Ultra-low power domain wall device for spin-based neuromorphic computing,” *ArXiv Prepr. ArXiv200712357*, 2020.
- [3] J. M. Lee *et al.*, “Field-free spin-orbit torque switching from geometrical domain-wall pinning,” *Nano Lett.*, vol. 18, no. 8, pp. 4669–4674, 2018.
- [4] P.-B. He, M.-Q. Cai, and Z.-D. Li, “Walker solution for a magnetic domain wall driven by spin-orbit torques,” *Phys. Rev. B*, vol. 102, no. 22, p. 224419, 2020.
- [5] I. Lemesh and G. S. D. Beach, “Walker Breakdown with a Twist: Dynamics of Multilayer Domain Walls and Skyrmions Driven by Spin-Orbit Torque,” *Phys Rev Appl*, vol. 12, no. 4, p. 044031, Oct. 2019, doi: 10.1103/PhysRevApplied.12.044031.
- [6] J. Linder and M. Alidoust, “Asymmetric ferromagnetic resonance, universal Walker breakdown, and counterflow domain wall motion in the presence of multiple spin-orbit torques,” *Phys. Rev. B*, vol. 88, no. 6, p. 064420, 2013.
- [7] V. Risinggård and J. Linder, “Universal absence of Walker breakdown and linear current-velocity relation via spin-orbit torques in coupled and single domain wall motion,” *Phys. Rev. B*, vol. 95, no. 13, p. 134423, 2017.